Journal of Applied Fluid Mechanics, Vol. 10, No. 5, pp. 1461-1474, 2017.
Available online at www.jafmonline.net, ISSN 1735-3572, EISSN 1735-3645.
DOI: 10.18869/acadpub.jafm.73.242.27541

Aerodynamically Efficient Rotor Design for Hovering Agricultural Unmanned Helicopter

B. A. Haider[1], C. H. Sohn[1†], Y. S. Won[2] and Y. M. Koo[2†]

[1] *School of Mechanical Engineering, Kyungpook National University, Daegu, 41566, Korea*
[2] *School of Agricultural Civil and Bio-Industrial Engineering, Kyungpook National University, Daegu, 41566, Korea*

†*Corresponding Author Email: chsohn@knu.ac.kr, ymkoo@knu.ac.kr*

(Received December 25, 2016; accepted May 14, 2017)

ABSTRACT

Unmanned aerial vehicles, especially agricultural unmanned helicopters (AUH), are nowadays extensively used in precision agriculture. AUHs have recently become responsible for spraying fertilizers and pesticides for crop yields. The strong downward rotating flow produced by the main rotor helps very uniform crop spraying which determines that how important is the aerodynamics of rotor blade in AUH. In this work, the aerodynamic performance of AUH rotor blades is evaluated and an efficient blade is obtained by numerically investigating the influence of design variables on the aerodynamics of rotor blades. The design variables consist of airfoil shape, pitch settings, and twist angle. The limited power available in hover and aerodynamic requirements (lift and drag) are the aerodynamic constraints. This analysis only considers the hovering flight condition at a constant rotational speed. The aerodynamically efficient rotor blade which is based on gradually varying and linearly twisted airfoil shapes, show a significant improvement in hover performance with relatively uniform blade loading. After testing, the optimum blade can be used as the main rotor in the AUH to perform precision farming.

Keywords: Agricultural unmanned helicopter; Airfoil; Computational fluid dynamics; Hover performance; Rotor blade optimization.

NOMENCLATURE

A	rotor disk area	R	rotor blade radius
C_P	rotor power coefficient	r	radial location along the blade radius
C_Q	rotor torque coefficient		
C_T	rotor thrust coefficient		
c	reference chord length of the rotor blade	θ_c	rotor blade collective pitch angle
C_p	pressure coefficient	θ_{tw}	rotor blade twist angle
FM	hovering rotor figure of merit	σ	rotor blade solidity
M_{tip}	tip Mach number	Ω	nominal rotational speed of rotor

1. INTRODUCTION

A desire to increase productivity and profitability in the agriculture has stimulated interest in innovative technologies. Advances in information technology and their application in crop production, which is labeled as precision agriculture (PA), is creating potential for substantial changes in management and decision making in the farming sector. Whelan and Taylor (2013) define the concept of PA as an approach to increase whole-farm productivity and profitability in an environment-friendly manner. Farmers use PA practices by applying precise and correct amounts of seed, water, pesticides, and herbicides at the right time, which benefits the entire crop cycle. Consequently, precision agriculture management has turned out to be a keystone of sustainable agriculture.

Indeed, PA is not based on a single technology, but an integration of various modern techniques. These include high precision positioning systems (e.g. GPS), geographical information systems (GIS), grain yield monitoring devices, sensors and remote sensing, variable-rate technologies, and crop management. Aerial systems such as satellites, air-craft, balloons, unmanned aerial systems (UAS), and rotorcraft are the common platforms used in data acquisition and field variability maps to support

decision making and management practices. The application of these airborne platforms significantly reduces the time necessary for surveying the land area, and consequently, allows farmers to adjust their agricultural practices. However, Stafford (2000) believes that the cost, availability, and processing of crop imagery from satellites and aircraft have made their applications limiting and impractical. As a result, UAS could be an economical, feasible, and potential substitute for high-resolution photography and spraying pesticides, more information can be found in Sugiura *et al*. (2005), Zhang and Kovacs (2012), Senthilnath *et al*. (2016).

In recent years, the application of UAS has flourished, ranging from fixed-wing aircraft to multicopters. Specifically, the AUH has been applied to agricultural use because heli copters have numerous benefits over fixed wing air craft, such as vertical take-off and landing (VTOL), hovering, low runway requirements, and the ability to fly at low speeds and altitude. AUHs are smaller than full-scale manned helicopters and readily used as a tool for crop status sensing.

In contrast to sophisticated applications of unmanned helicopters, AUHs have also been used for chemical spraying (Koo *et al*. 2006 a, Meng 2015). Applying pesticides manually is a very labor intensive, inefficient, and hazardous job for the operators. However, aerial application of chemicals with an AUH ensures accurate and timely spraying, decreases the drift potential and evaporation, and reduces the environmental impact. In addition, the rotor downwash generated while hovering results deep penetration of the chemical and ensures uniform application.

Helicopters are available in a range of shapes and sizes, but most share the same major parts. All parts of a helicopter are important, but main rotors are the most important (Prouty 2009) because they develop aerodynamic lift. Accordingly, the aerodynamicists take special care in the aerodynamic design of the main rotor to ensure the optimum performance both in hover and cruise flight conditions.

For aerial applications, the agricultural helicopters operate at a relatively low speed (4 m/s to 7 m/s) and altitude (Koo *et al*. 2006); therefore, the aerodynamics of AUHs could be considered as nearly hovering.

The objectives of this research are threefold. We aim to: (1) conduct a performance evaluation of three different rotor blade configurations (two basic plus one gradually varying airfoil section) for a range of collective pitch angles, (2) conduct an investigation of the rotor efficiency improvement and aero-loads by linearly changing the pitch angle of airfoil sections along the radius, i.e., blade twist angle, and (3) select the most efficient rotor blade among the designed configurations at a limited actual power available and at maximal thrust conditions.

This study is based on computational fluid dynamic (CFD) simulations for a constant angular blade rotation in hovering flight. To establish the accuracy of the CFD method in hover performance prediction, a baseline rotor, experimentally tested by Caradonna and Tung (1981) is used.

2. COMPUTATIONAL METHODOLOGY

The accurate and reliable computation of the helicopter rotor performance continues to be a challenge in rotorcraft design. A variety of numerical techniques can be utilized in making this assessment, ranging from the simplified momentum theory to direct modeling using advanced computational fluid dynamics (Miller 1985, Conlisk 2001, Leishman 2006, Johnson 2013). The methods based on the momentum theory are low-fidelity methods while for better accuracy, high-fidelity methods such as CFD are desired.

CFD has matured as a general predictive tool with sensible reliability in the industry (Moin and Kim 1997, Xia and Sun 2002, Lee *et al*. 2013, di Perta *et al*. 2016). Since the first application of CFD to the rotary wing (Caradonna and Isom 1972), recent solutions of Reynolds-Averaged Navier-Stokes (RANS) equations offer substantial developments in the computation of complex aero-dynamics around the rotorcraft (Ahmad and Duque 1996, Pomin and Wagner 2002, Costes *et al*. 2012, Kranzinger *et al*. 2016) and the similar applications (Adeeb *et al*. 2016). In this paper, a CFD-based methodology is adopted to simulate the aero-dynamic characteristics, and therefore, the performance of hovering AUH rotor blades. The details of the applied method are discussed in the subsequent sections.

2.1 Agricultural Unmanned Helicopter

The AUH employed in the performance evaluation is a two-bladed AgroHeli-4G (AH-4G), a prototype designed and constructed by Kyungpook National University (Koo 2009). It is shown in Fig. 1. The total lift capacity of AH-4G is up to 1176 N with an engine power of 25 kW. To improve the performance of the AH-4G; airfoil shape, collective pitch, and blade twist are the parameters considered for the simulation. The characteristics of the AUH test bed are listed in Table 1.

2.2 Flow Physics Solver

The computations are performed using the Ansys Fluent Release 16.2 solver. A multiple reference frame (MRF) method (Luo and Gosmans 1994) is employed to simulate the isolated rotating blades. The isolated rotor in hovering flight exhibits a steady-state flow in the moving reference frame (Pomin and Wagner 2002); therefore, the equations of motion are modified to compute the steady-state solution. The modification incorporates the additional acceleration terms that occur due to the transformation from the stationary to the moving reference frame. The MRF method is a steady state approximation, and the flow in each moving cell zone is solved using the moving reference frame equations while the stationary equations are used to solve the stationary zone ($\Omega = 0$). A local reference frame transformation is performed at the interfaces between adjacent cell zones to enable flow variables

Fig. 1. The agricultural unmanned helicopter for a test bed.

in one zone to be used to calculate fluxes at the boundary of the adjacent regions. In this study, the steady viscous flow fields are computed over an isolated rotor blade by solving the NavierStokes equations using the MRF method.

Table 1 Characteristics of the test bed (AgroHeli-4G)

Parameters	Symbols	Values
Number of blades	N_b	2
Rotor blade radius	R	1.510m
Blade chord length	c	0.135m
Nominal rotor speed	Ω	890 rpm
Blade tip Mach number	M_{tip}	0.414
Blade aspect ratio	AR	10.0
Rotor solidity	$\sigma = \frac{N_b c}{\pi R}$	0.0569
Rated power available	p_{av}	25kW
Total dead weight	W_d	650N

The governing equations of fluid flow for a steadily moving frame can be written as follows

conservation of mass:

$$\frac{\partial \rho}{\partial t} + \nabla . \rho \overrightarrow{v_r} = 0 \quad (1)$$

conservation of momentum:

$$\frac{\partial}{\partial t} \rho \vec{v} + \nabla . (\rho \overrightarrow{v_r} \vec{v}) + \rho [\vec{\omega} \times (\vec{v} - \overrightarrow{v_t})] = -\nabla p + \nabla . \bar{\bar{\tau}} + \vec{F} \quad (2)$$

conservation of energy:

$$\frac{\partial}{\partial t} \rho E + + \nabla . (\rho \overrightarrow{v_r} H + \rho \overrightarrow{u_r}) = \nabla . (k \nabla T + \bar{\bar{\tau}} . \vec{v}) + S_h \quad (3)$$

where ρ is the fluid density, $\vec{v}_r$ is the relative velocity (the velocity viewed from the moving frame), $\vec{v}$ is the absolute velocity (the velocity viewed from the stationary frame), $\vec{v}_r$ is the translational frame velocity, $\vec{\omega}$ is the angular velocity, $\bar{\bar{\tau}}$ is the viscous stress tensor, p is the fluid pressure, $\vec{F}$ represents the external body force, E is the internal energy, H is the total enthalpy, and $\overrightarrow{u_r} = \vec{v}_r + \vec{\omega} \times \vec{r}$ is the velocity of the moving frame relative to the inertial reference frame.

The purpose of the energy Eq. (3) in this simulation is to provide temperature to compute the density using ideal-gas law, since, pressure far-field boundary condition is used at the boundaries of the stationary zone.

2.3 Geometry Modeling and Boundary Conditions

The blade configurations are categorized as (A) configuration 1 (C1): V1505A airfoil is used throughout the blade radius, (B) configuration 2 (C2): V2008B airfoil is used both at inboard and outboard blade sections, and (C) configuration 3 (C3): V1215C, airfoil sections gradually vary from V1505A (inboard) to V2008B (outboard). The airfoil sections used are superimposed in Fig. 2. The summary of airfoil geometric parameters as a fraction of chord length (0.135 m) is provided in Table 2.

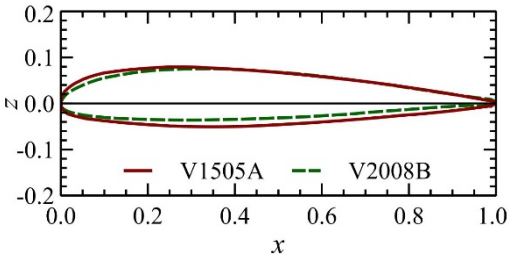

Fig. 2. An overlay of rotor blade sections, normalized by the chord length.

The AUH rotor consists of two blades of rectangular planform with a root cutout at the grip section, and a parabolic-shaped tip section. The blade geometric model is presented in Fig. 3(a). The blade is parametrically modeled in Ansys Design Modeler

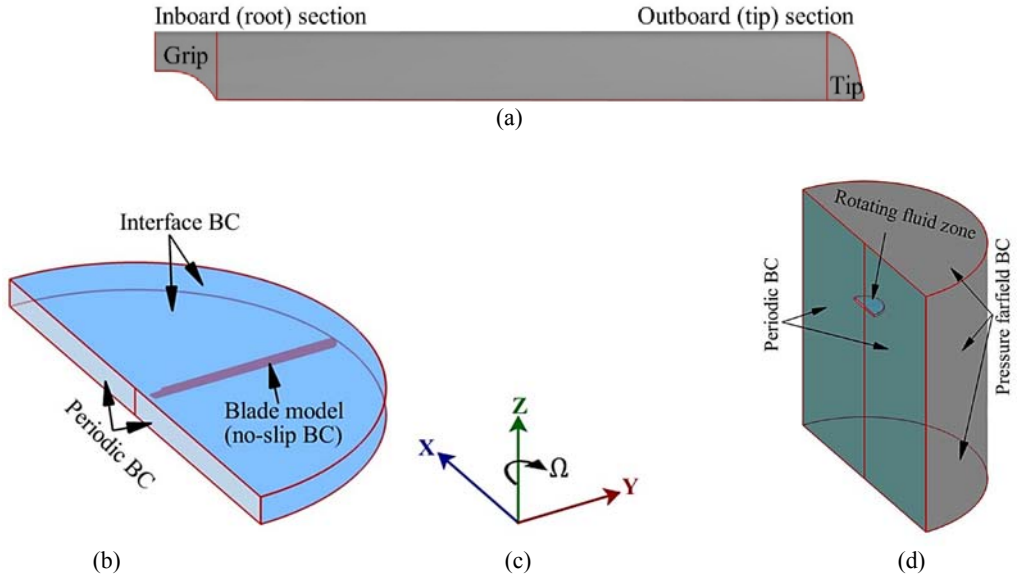

Fig. 3. Geometry modeling, computational domain, and boundary conditions for the rotor simulations: (a) Rotor blade, (b) Rotating fluid zone, (c) Axis system, and (d) Stationary fluid zone.

Release 16.2, which allows the modification of various rotor blade parameters, such as airfoil section or blade pitch angle (θ_c). In untwisted configurations, both the inboard and outboard sections have the same pitch angle, whereas in twisted configurations the pitch angle is linearly varied from the root (higher angle) to tip (lower angle). It is considered that the reference section with zero twist is located at r/R = 0.80 (cf. Sec. 2.5). The blade has an aspect ratio of 11.185, which is the ratio of the radius and the reference chord at r/R = 0.80. Table 3 summarizes the design variables used in evaluation of the optimum AUH rotor blade configuration, along with their designations. The configurations are identified by their designations in the subsequent deliberations.

The computational domain for the AUH rotor blade consists of a half cylinder and a single blade contained in a circular disk. This virtual disk is the rotating fluid zone. The rest of the computed domain (cylindrical volume) is the stationary fluid zone. The second blade is considered by using the rotational periodic boundary condition to save computational time and resources. The blade model and the rotating and stationary fluid zones and their corresponding boundary conditions are illustrated in Fig. 3. The center of rotation lies at (x = 0, y = 0, z = 0) with the x-axis pointed from the leading edge towards the trailing edge of the blade, the y-axis is positioned along the blade span, and the z-axis is pointed upward (Fig. 3(c)). The moving fluid volume is rotating clockwise with a rotational speed (Ω) of 890 rpm about the z-axis. Furthermore, the farfield boundary is located at 7.5R in the radial direction, the upper boundary (positive z-direction) is placed at 5.0R and the lower boundary (negative z-direction) is positioned at 12.5R. The ambient conditions are imposed at the farfield boundary of the stationary cell zone, whereas the blade surface is modeled as an adiabatic no-slip wall. However, an interface boundary condition is applied to separate the rotating and static cell zones.

Table 2 Geometric characteristics of airfoil sections (fraction of the chord length)

Parameters	V1505A	V2008B
Maximum thickness	0.179	0.131
Maximum camber	0.020	0.027
Maximum thickness location	0.301	0.328
Maximum camber location	0.171	0.334
Leading edge radius	0.028	0.014

2.4 Grid Generation, Physical Solver, and Convergence Criteria

The unstructured grid method is adopted to mesh the computational domains. Unstructured meshing provides flexibility in grid generation and is widely used in helicopter rotor blade simulations in hovering flight (Lee and Kwon 2006). The surface of the rotor blade is meshed with unstructured triangular elements where the size of each triangle is defined by a base size of 0.005c and prism layers are applied to capture the boundary layer such that 5 < wall y+ < 250. The computations used for prism layer growth are as follows

$$H_p = h \times g^{n-1} \tag{4}$$

where Hp is the height of the last prism, h = 0.001c is the height of the first layer, g = 1.2 is the growth rate, and n = 10 is the number of layers. The grid is also refined in the wake region. To obtain the grid independent solution, mesh sensitivity is also studied with three grid sizes of 1.2, 2.4, and 4.8 million elements. For each grid size (coarse, medium, and

Table 3 Summary of design variables used to evaluate an optimum rotor blade configuration

Configuration (Nominal Id)	Airfoil sections		Collective pitch angle,θ_c				
			Untwisted		Twisted		
	Inboard	Outboard	Inboard	Outboard	Inboard	r/R=0.8	Outboard
C1 (V1505A)	V1505A	V1505A	6° *to* 20°	6° *to* 20°	10° *to* 24°	6° *to* 20°	5° *to* 19°
C2 (V2008B)	V2008B	V2008B					
C3 (V1215C)	V1505A	V2008B					

(a) Rotor blade surface mesh

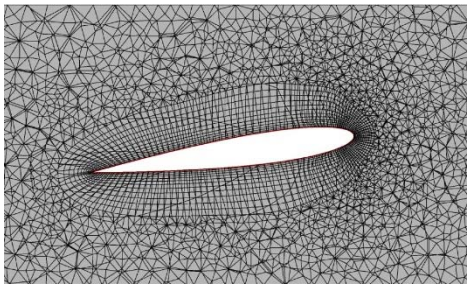

(b) Mesh projection on a plane at r/R = 0.8

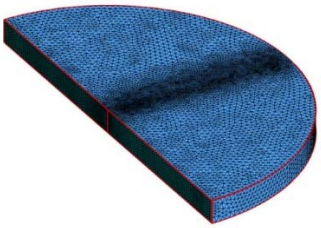

(c) Rotating fluid zone

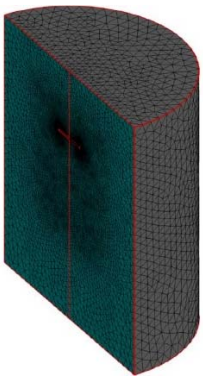

(d) Stationary fluid zone

Fig. 4. Surface and volume unstructured grids.

fine), the mesh parameters for rotor blade remains the same. The grid size of 2.4 million elements is used for the AUH rotor blade simulations. Fig. 4 shows the surface and volume unstructured meshes.

The physical model of turbulence is the realizable k-epsilon (Rkε) with enhanced wall treatment. However, the effect of various turbulence models is also investigated (cf. Sec. 2.7). For the solution controls, the coupled algorithm is used for pressure and velocity coupling. The second order discretization scheme is utilized for the pressure equation, and the second-order upwind scheme for the density, momentum, and energy equations is employed. The residuals of continuity and momentum are defined as Ansys Fluent Release 16.2 and set to five orders of magnitude to acquire a sufficiently converged solution. The values of important variables like lift and drag are also monitored, and their convergence is also adequately ensured.

2.5 Variation in Blade Pitch Angle

In a rotating blade, each element of the blade travels at a different speed, which affects the contribution of lift and drag at every point on the blade. Subsequently, the lift distribution is not uniform along the blade span, which is not desirable. To realize uniform loading, blades are twisted such that the local angle of attack increases when traveling towards the root section. The effect of rotor blade twist is analyzed (by comparing with untwisted rotor) as a distribution of the aeroloads over the rotor surface along the radius. The rotor blade loading is the ratio of the thrust coefficient (C_T) to solidity ($\sigma=N_b c/\pi R$), where N_b is the number of blades, c is the blade chord, and R is the blade radius.

The rotor blades are twisted along the span with a variation in the blade pitch on the root as $\Delta\theta = \theta_{tw} r$, where θ_{tw} is the tip pitch minus the root pitch, and r is the fraction of the blade radius. The value of r is 0.0 at the inboard station and 1.0 at the outboard station. The relation $\theta_c(r) = \theta_0 + r\theta_{tw}$ computes the pitch angle at the reference position, where θ0 is the reference pitch. The pitch angle at the inboard station is varied from 10° to 24°, and the angle is ranging from 5° to 19° at the outboard section. The difference between the tip and the root pitch gives the twist of the blade ($\theta_{tw} = -5^\circ$) while 0° for the untwisted blade. The pitch angle at 80% of the blade length is used as a reference to compare hover performance.

2.6 Hover Performance Parameters

Hover is a flight regime in which the thrust generated by the rotor blades just offsets the weight. The primary design parameters for the helicopter are the dimensionless coefficients related to thrust and

power (Conlisk 2001). These coefficients are: the thrust coefficient defined by

$$C_T = \frac{T}{\rho A(\Omega R)^2} \quad (5)$$

the torque coefficient defined by

$$C_Q = \frac{Q}{\rho A(\Omega R)^2 R} \quad (6)$$

and the power coefficient defined by

$$C_P = \frac{P}{\rho A(\Omega R)^3} \quad (7)$$

where P(= ΩQ ∴ $C_P = C_Q$) is the rotor power required to produce thrust T , Q is the rotor torque, ρ is the fluid density, A, is the disk area, Ω is the angular velocity of the rotor, and R is the distance from the axis of rotation to the blade tip. The power required to turn the main rotor in hovering is composed of induced power and profile power (to overcome viscous losses at the rotor). These components of the required power are mainly affecting the blade aerodynamic design and hover performance (Leishman 2006).

The hover efficiency of rotor blades is determined by the figure of merit (FM), which is particularly valuable when comparing rotors with different air-foil shapes and when investigating the influence of other design variables, such as the blade twist. This quantity is defined as the ratio of the ideal power (P_I) required to produce the thrust and the actual total power required (P_A).

$$\text{FM}=\frac{P_I}{P_A} = \frac{C_T^{1.5}}{\sqrt{2}C_P} = \frac{C_T^{1.5}}{\sqrt{2}C_Q} \quad (8)$$

2.7 Validation of the CFD Method

It is essential to conduct the validation study to establish the accuracy and reliability of the CFD method when no experimental data exists for the problem in question (Roache 1997, Celik *et al*. 2008). Therefore, in the present work, experimental data from the Caradonna and Tung (1981) rotor are utilized to validate the CFD methodology. This benchmark case is used extensively in the rotorcraft community for the validation of computational methods. Table 4 lists the geometric and simulation parameters of the banchmarked rotor blade.

Table 4 Summary of geometric and simulation parameters for the experimental rotor

Parameters	Values
Rotor blade diameter, D	2.286m
Nominal rotor speed, Ω	1250pm
Blade tip Mach number, M_{tip}	0.439
Blade chord length, c	0.1905m
Blade aspect ratio, AR	6.0
Blade twist, θ_{tw}	0°
Blade collective pitch, θ	8°
Number of blades, N_b	2
Blade airfoil section	NACA0012

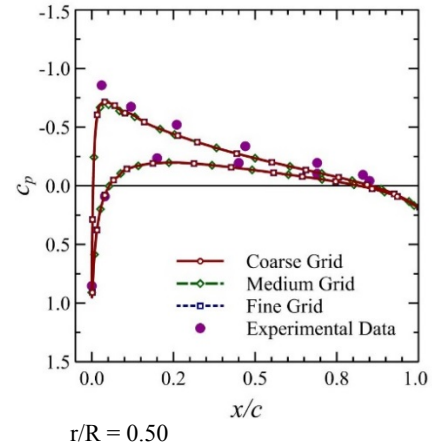

(a) r/R = 0.50

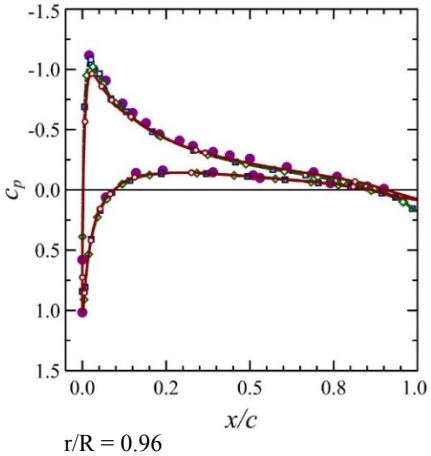

(b) r/R = 0.96

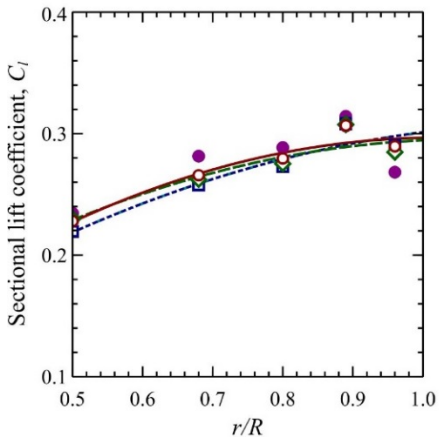

(c) Section lift coefficient

Fig. 5. Comparison of computed surface pressure (a) r/R = 0.50; (b) r/R = 0.96, and section lift coefficients with experimental data of Caradonna and Tung (1981) for grid sensitivity study at $\theta_c = 8^\circ$, Ω = 1250rpm (M_{tip} = 0.439).

Ideally, the simulation results should be independent of the computational grid. Therefore, to achieve grid independence, three meshes are considered with corresponding grid numbers of 1.2 (coarse), 2.4 (medium), and 4.8 (fine) million. The grids are refined such that the solution is in the asymptotic range of convergence (Roache 1997, Roache 1994). The Rkε model is used to perform the grid sensitivity study.

Table 5 Grid sensitivity study

G1, G2, G3 (coarse, medium, fine)	1202427, 2403905, 4791704
Grid refinement ratio, r	2.00
Computed thrust coefficient, ($CT \times 10^{-2}$)	0.400, 0.428, 0.430
Experimental thrust coefficient, ($CT \times 10^{-2}$)	0.459
Percentage difference	13.7%, 7.0%, 6.5%
Fine-grid convergence index, GC I_{12}	0.045%

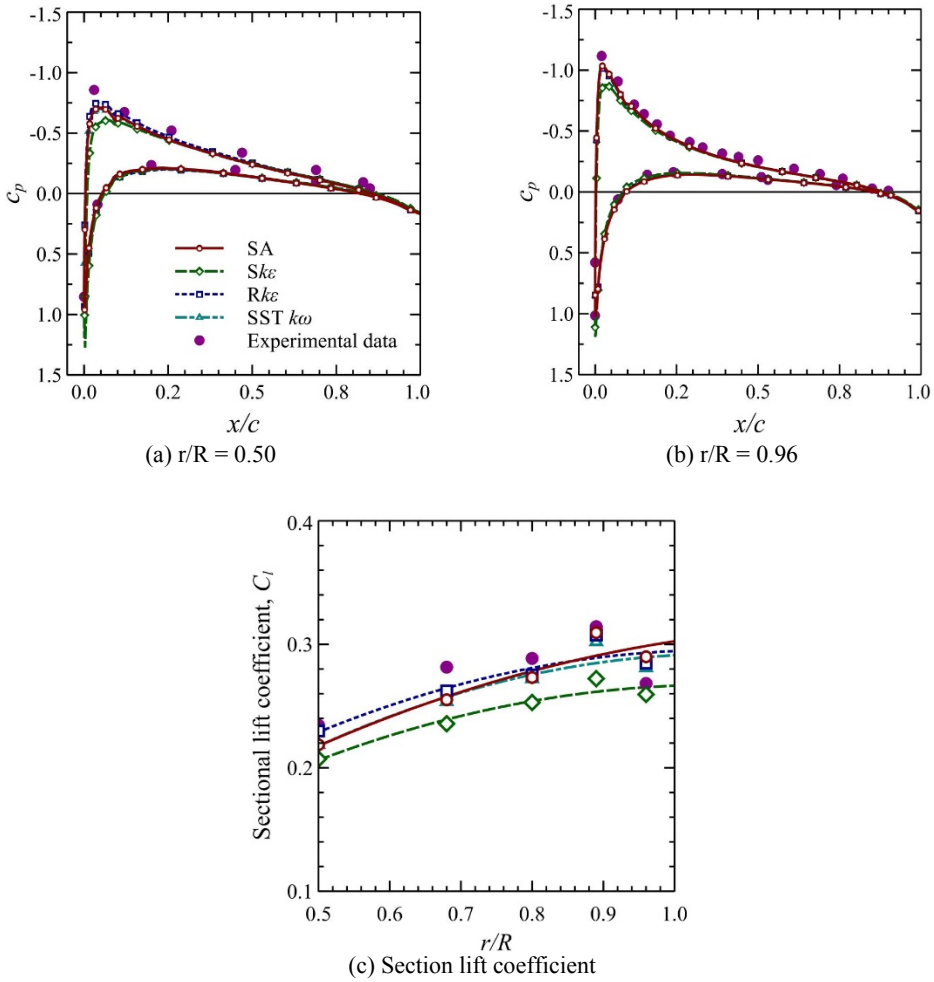

Fig. 6. Comparison of computed surface pressure (a) r/R=0.50; (b) r/R=0.96, and section lift coefficients with experimental data of Caradonna and Tung (1981) for various turbulence models at θc=8°, Ω=1250rpm (Mtip=0.439).

Table 5 indicates the grid statistics and the resulting thrust coefficient computed by using the parameters reported in Table 4. The convergence of each simulation is adequately ensured (see Sec. 2.4). Based on the simulation results of grid independence (Table 5), the numerical uncertainty in the fine-grid solution for the thrust coefficient is reported as 0.045%.

Figures. 5(a) and 5(b) compare the chordwise surface pressure distribution (cp) for each grid at two radial stations (i.e. r/R = 0.50 and r/R = 0.96), and all are in good agreement with the experimental data. The coefficient of pressure, cp, can be computed as $(2(p-p_\infty))/(\rho(\Omega R)2)$, where p_∞, p, ρ, and ΩR are the free stream pressure, fluid static pressure, fluid density, and the tip speed, respectively. Furthermore, Fig. 5(c) shows the loading distribution (section lift coefficient) along the radius of the blade, which exhibits a small deviation from the experimental

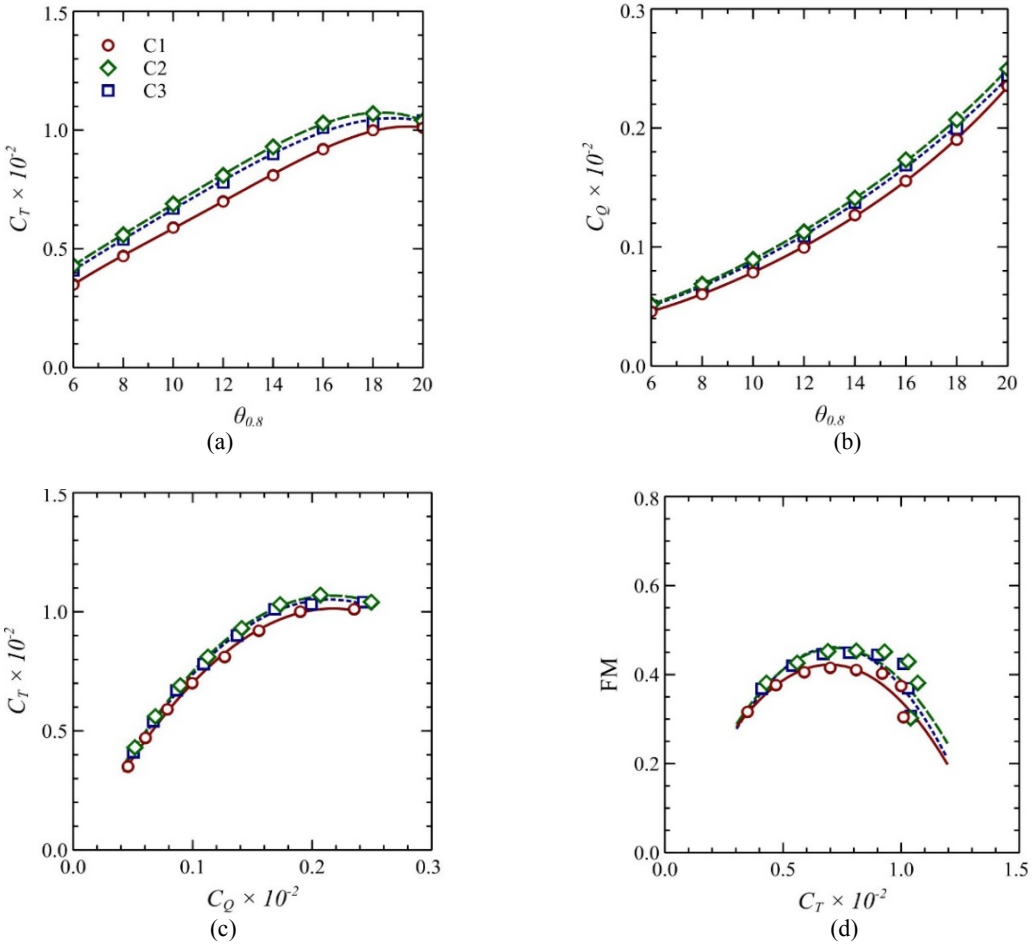

Fig. 7. Effect of airfoil shape and pitch settings on hover performance of rotor blade configurations at $\theta_{tw} = 0^\circ$ and $\Omega = 890$rpm (Mtip = 0.414).

data. Despite the fact that Fig. 5 depicted an agreement of plotted quantities with the experiment for all mesh sizes, the medium sized mesh is used for the subsequent simulations. The percentage difference in the case of coarse and fine grid solutions is 13.7% and 6.5%, respectively, when compared with the experiment. A comparatively small difference between medium and fine grid solutions indicates that the medium grid offers the best compromise between accuracy and the time required per simulation, and also entailed less computational resources. Hence, the medium grid is utilized for the subsequent CFD analysis.

The helicopter flowfield is turbulent; therefore, it is necessary to choose an appropriate turbulence model to simulate the flow physics accurately. For this purpose, three turbulence models are considered, including one-equation Spalart-Allmaras (SA), two-equation k-epsilon (standard (Skε) and realizable (Rkε)), and the shear-stress transport k-omega (SST − kω) model. Figs. 6(a) and 6(b) present the effect of turbulence models on the chordwise pressure distribution at two radial sections. All models except Skε show good agreement with the experimental pressure distribution for both of the sections. The Skε model has some discrepancies at the suction side of the blade near the leading edge where the pressure coefficient is under predicted. Fig. 6(c) compares the sectional lift coefficient for all turbulence models quantitatively. However, the difference is small among the candidate turbulence models except for Skε, but Rkε shows good agreement with the experiment, hence, Rkε is used for further simulations.

3. RESULTS AND DISCUSSION

The AUH rotor configurations are evaluated by computing the aerodynamic coefficients, including lift, drag, and moment. These aerodynamic quantities are then used to determine the thrust, power, and torque required for a particular flight regime. In hovering, the thrust is entirely related to the lift force, as it overcomes the helicopter weight and the drag is mainly induced drag incurred while the blades are producing lift. An important consequence of providing thrust is torque. The torque is directly related to the amount of engine power being used to turn the main rotor system. The rotor design pursues a maximal lift for a corresponding power source. Oftentimes the required power level is limited by a choice of aeronautical power supply due to its availability; therefore, the power limit should be considered in the

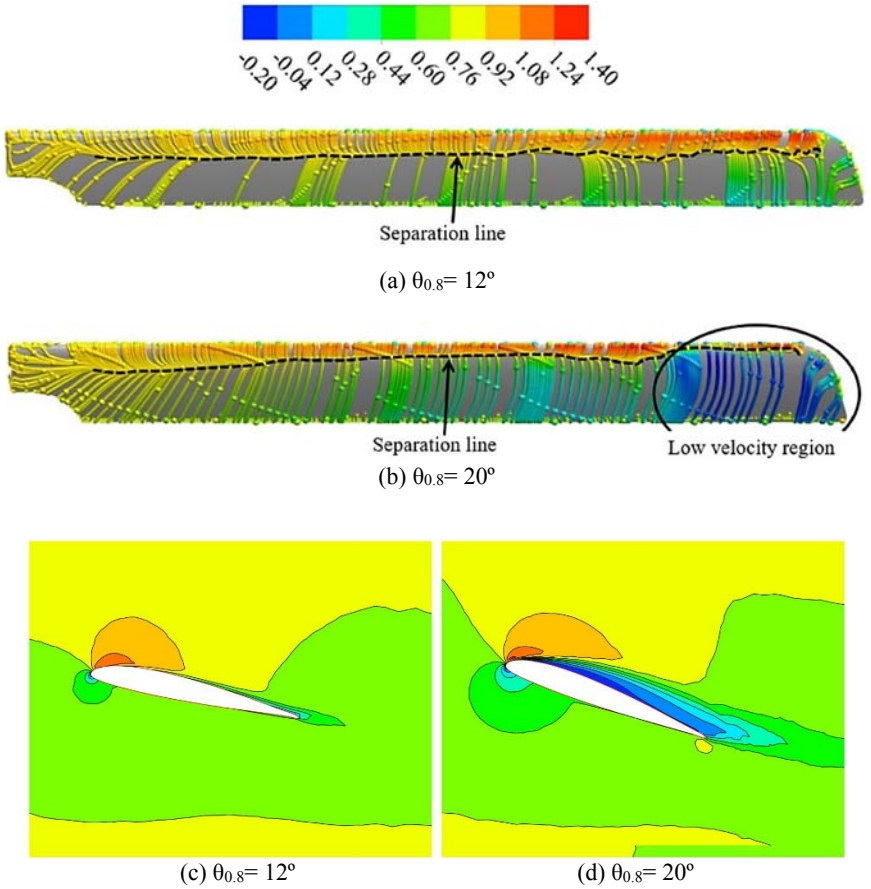

(a) $\theta_{0.8}$= 12º

(b) $\theta_{0.8}$= 20º

(c) $\theta_{0.8}$= 12º (d) $\theta_{0.8}$= 20º

Fig. 8. (a) and (b) surface streamlines colored by velocity; (c) and (d) contours of flow velocity at r/R=0.8 (normalized by the tip speed) for C3 at θ_{tw}=0° and Ω=890rpm (M_{tip} = 0.414).

Table 6 Summary of optimum performance parameters for rotor blade configurations

Parameters	C1		C2		C3	
	Untwisted	Twisted	Untwisted	Twisted	Untwisted	Twisted
Peak FM	0.4153	0.4526	0.4531	0.4820	0.4486	0.4753
C_T at peak FM	0.0070	0.0075	0.0080	0.0085	0.0078	0.0083
$C_{Q,opt} = C_{P,opt}\,(\times 10^{-2})$	0.0995	0.1023	0.113	0.1146	0.1090	0.1116
θ_{opt} at Peak FM	12°	13°	12°	13°	12°	13°
$\theta_{\max}$ *at* $C_{T,\max}$	20°	18°	18°	18°	20°	20°

design of the rotor, as well as the performance. Moreover, the hover performance for the configurations is calculated by plugging the aerodynamic parameters into Eqs. (5) to (8). Koo (2012) has already discussed the two-dimensional aerodynamic characteristics of the airfoil sections, but three-dimensional aerodynamic characteristics are yet to be analyzed. These characteristics are deliberated subsequently.

3.1 Effect of Airfoil Shape and Pitch Settings

The effect of airfoil shape and pitch settings on the hover performance of rotor blades when no twist is applied is presented in Fig. 7 as thrust-collective, torque-collective, thrust-torque, and figure of merit-thrust plots. The coefficient of thrust increases with the increase in pitch angle, and the maximum value is attained at 18°, as shown in Fig. 7(a). Afterward, the thrust starts decreasing for C1 and C2 as a consequence of the stall, while the thrust for C3 remains the same until 20°, after which stall may occur. In the case of C1 and C2, the stall begins due to the substantial deceleration in the flow, which is unable to support the boundary layer, hence, the flow separates from the airfoil surface (Fig. 8). The

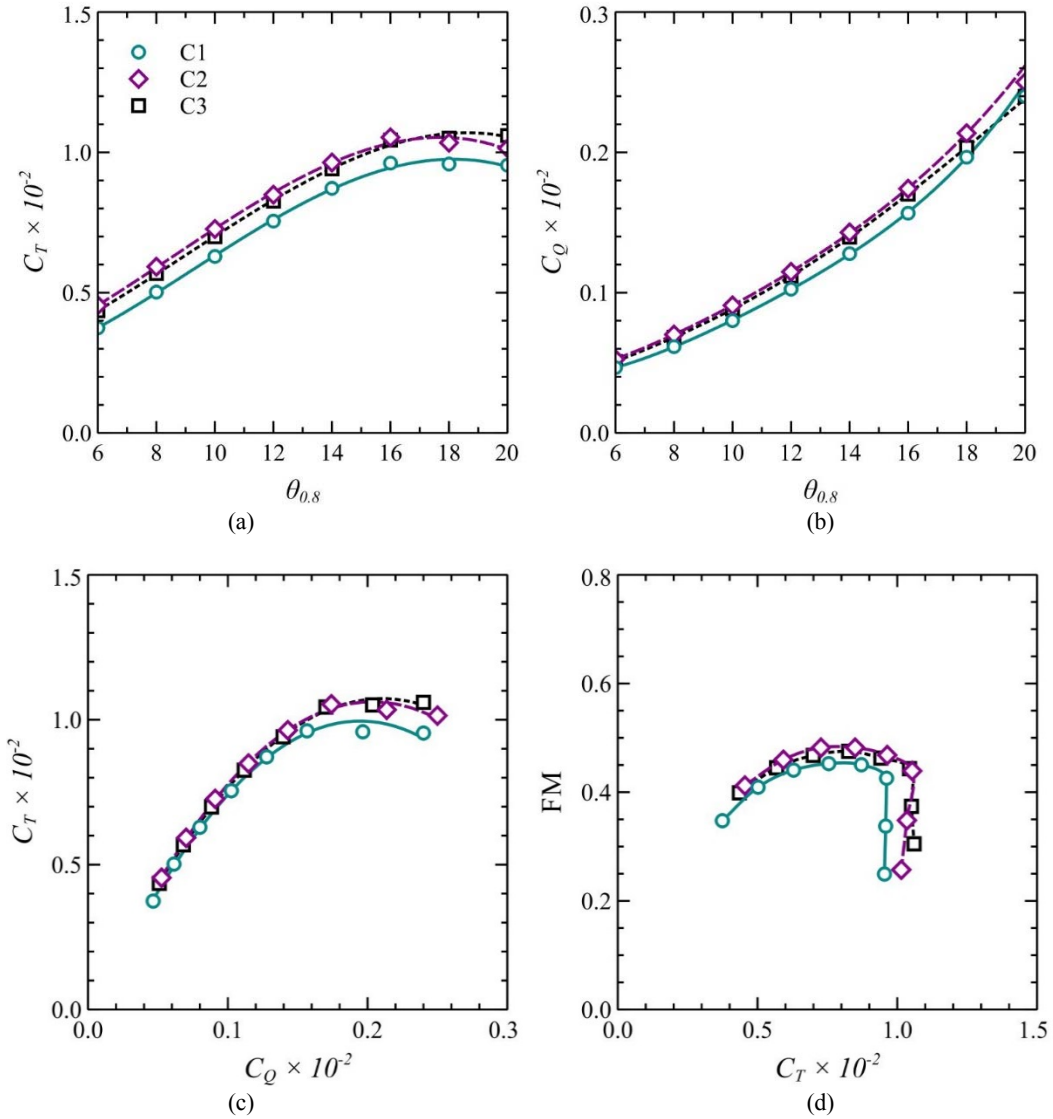

Fig. 9. Combined effect of blade twist, airfoil shape, and pitch settings on hover performance of rotor blade configurations at $\theta_{tw} = -5^{\circ}$ and Ω = 890rpm (Mtip = 0.414).

maximum value of lift at the stall is primarilydependent on the airfoil shape, Mach number, and the flow Reynolds number.

Even the rotors encounter a decrease in thrust at a higher pitch angle; the torque coefficient continues to increase as shown in Fig. 7(b). The continuous increment in the torque is a result of an increase in induced power, which is a consequence of high induced drag at higher angles of attack. Since torque (Q) is related to power (P = ΩQ), more power is required to turn the main rotor with the increase in torque due to the stall at a constant angular speed. Fig. 7(c) correlates the thrust with the amount of torque or power, which indicates an increase in power requirements. However, the blade stall limits the aerodynamic performance of the blade, and therefore, less thrust is produced.

The figure of merit (FM) as a function of the thrust coefficient for the rotors in question is presented in Fig. 7(d). The hover efficiency increases steadily and approaches a peak value at moderate thrust and then gradually drops. The peak value of FM corresponds to the optimum pitch angle (θopt , please refer to Table 6). It is determined from Figs. 7(a) and 7(d) that the useful range of pitch angles of all rotor blades is between 10° to 14°.

Nevertheless, the untwisted configurations exhibit similar aerodynamic behavior. Still, there exists an improvement in the aerodynamic performance when compared to the rotor blades having different airfoil shapes. Configuration C2 can produce 14% more thrust than C1 and 2.8% more thrust than C3. C2 is comprised of a relatively more cambered airfoil section which exhibits more lift (thrust) and hence more drag (power required). Based on the figure of merit, C2 is 9% more aerodynamically efficient than C1, which is one percent more efficient than C3. A relatively small difference exists between C2 and C3 because the driven region in rotating blades is

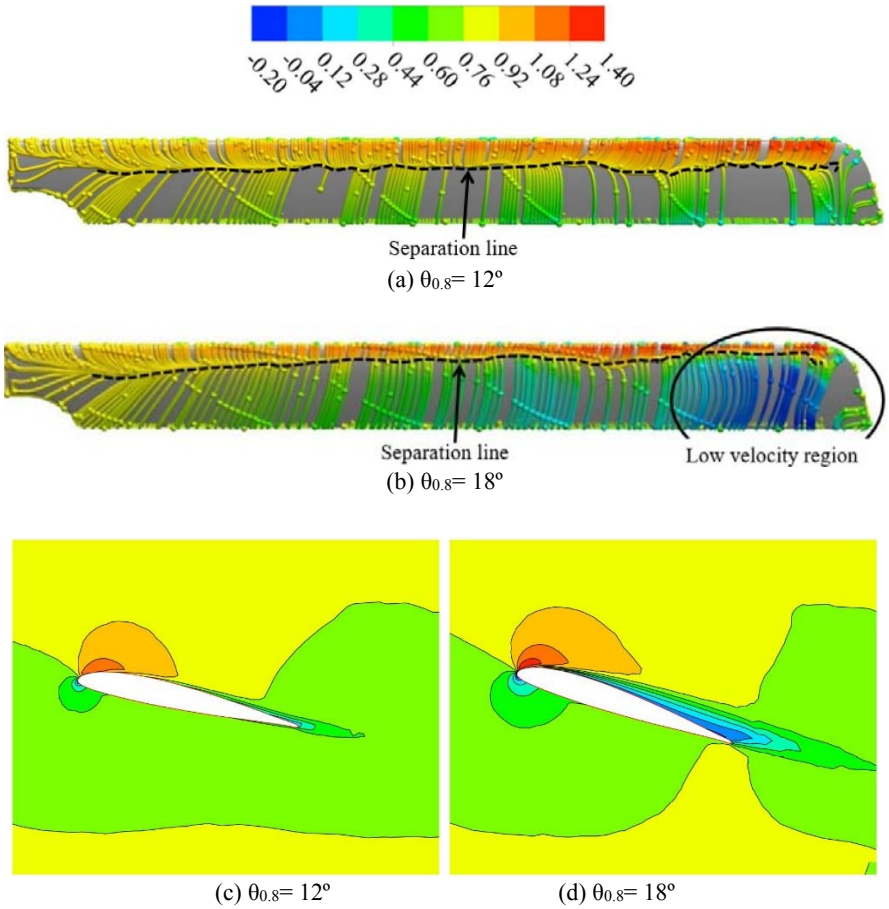

Fig. 10. (a) and (b) surface streamlines colored by velocity; (c) and (d) contours of flow velocity at r/R=0.8 (normalized by the tip speed) for C3 at θ_{tw} =−5° and Ω=890rpm (Mtip=0.414).

between 25% to 75% of the blade radius when hovering. Therefore, towards the outboard region, the aerodynamics of the airfoil section with higher camber is dominated, which yields overall an improved configuration (C2) with added hover efficiency compared to C1. this indicates that the inboard section of the rotor blade has a minor influence on the blade efficiency.

The qualitative results for C3 at two different pitch angles (i.e. 12° and 20°) are presented in Fig. 8. The flow streamlines on the surface of the rotor blade indicate a forward movement of the separation line at a higher angle (Fig. 8(b)) when compared to streamlines at a lower angle (Fig. 8(a)). The flow over the blade surface at 20° is separated at the leading edge near the tip region, as shown in Fig. 8(b), which shows the phenomenon of the tip stall happens earlier than the inboard region. In the case of stall occurrence, a low-velocity region appears near the outboard section, which degrades the overall blade performance. The normalized velocity contours at 80% of the blade span are illustrated in Figs. 8(c) and 8(d). Most of the flow is attached at 12°, whereas the separation occurs at the leading edge in the case of higher pitch angle. For simplicity, the qualitative results are discussed only for C3. However, C1 and C2 have similar flow characteristics when comparing the low and high pitch angles.

3.2 Effect of Twist Angle

The combined effect of blade twist, airfoil shape, and pitch variation on the aerodynamic efficiency of rotor blades is presented in Fig. 9. The pitch angle of the blades linearly varied to achieve a negative twist of 5° (cf. Sec. 2.5). The performance is evaluated in a similar way as discussed in the previous section for untwisted configurations. The correlation between thrust and blade pitch is non-linear, as shown in Fig. 9(a), and a gradual stall is observed in the case of twisted blades. The required power is increased even after the stall due to the significant contribution of the profile drag, which is reflected in the torque coefficient; see Fig. 9(b). Fig. 9(c) describes the relation between thrust and torque (power). The larger the thrust, the larger the torque is required for blade rotation. The figure of merit as a function of the thrust coefficient for the twisted rotors is plotted in Fig. 9(d). The hover efficiency increases gradually and approaches a peak value at moderate thrust and then suddenly drops. Figs. 9(a) and 9(d) set the useful range of pitch angles of twisted rotor blades as 10° to 16°.

Table 7 Summary of operating performance parameters at a limited power of 25 kW (C_P=0.001)

Parameters	C1		C2		C3	
	Untwisted	Twisted	Untwisted	Twisted	Untwisted	Twisted
C_T	0.0070	0.0074	0.0074	0.0078	0.0074	0.0077
$\theta_{0.8}$	12.0°	11.8°	10.9°	10.8°	11.2°	11.0°
FM	0.4153	0.4520	0.4526	0.4820	0.4481	0.4735

Table 8 Summary of operating performance parameters at the maximal lift (C_T=0.01)

Parameters	C1		C2		C3	
	Untwisted	Twisted	Untwisted	Twisted	Untwisted	Twisted
$C_Q = C_P (\times 10^{-2})$	0.1870	_	0.1608	0.1530	0.1652	0.1550
$\theta_{0.8}$	17.8°	_	15.3°	14.7°	15.8°	15.1°
FM	0.3755	_	0.4400	0.4610	0.4255	0.4550

Figure 10 presents the physical flow behavior of twisted C3 for low (12°) and high (18°) pitch angles. The flow separates near the leading edge of the blade at a higher angle (Fig. 10(b)), while the flow remains attached in the case of a small pitch angle (Fig. 10(a)). A low-velocity region is also observed near the blade tip, which is an indication of tip stall; see Fig. 10(b). A substantial loss in the lift and a sharp increase in the drag are the consequences of the stall. The maximum thrust produced is limited by a significant decrease in the lift due to stall. The power requirement also increases with a sudden increase in drag. Therefore, stall deteriorates the rotor blade performance and may be avoided by applying stall delay techniques. The velocity contours at 80% of the blade radius normalized by the tip speed are shown in Figs. 10(c) and 10(d), which compares the flow characteristics at low and high pitch angles, respectively.

Figure 11 shows the spanwise variation of section thrust loading for C3. For comparison purposes, the collective pitch of each case is adjusted iteratively so that the resulting thrust coefficient for the untwisted and twisted case is approximately the same. The peak radial loading is slightly beyond 0.80R for both cases. With twist, the aerodynamic loads become more uniform along the blade radius, except for inboard and outboard load peaks. As the twist distribution is driven linearly, Fig. 11 clearly shows a reduction in thrust loading near the tip region. Moreover, the associated small blade loads at the outboard can prevent an instantaneous tip stall. Furthermore, the twist also helps with the reduction of induced and profile drag losses that may be realized with a more uniform inflow.

The optimum hover performance parameters for both the untwisted and twisted blades are compared in Table 6, which indicate a 6% improvement in the hover efficiency for each configuration when the blades are twisted. The airfoil shape also has a positive effect on the hover performance. In the case of untwisted configurations, C2 and C3 exert 5.7%more thrust than C1 at optimal values of the FM. The twisted configurations, C2 and C3, are 10.8% greater in thrust than that of C1, and the FM is also close to the optimum values.

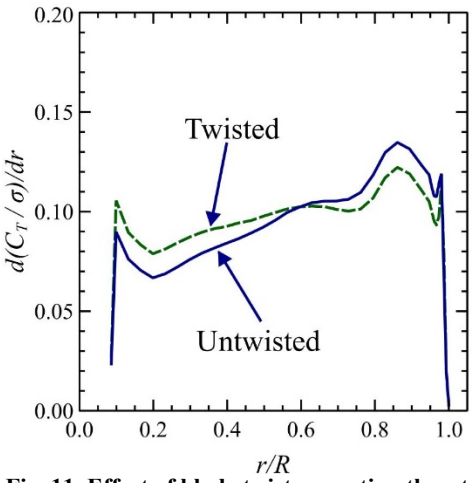

Fig. 11. Effect of blade twist on section thrust coefficient for configuration C3.

3.3 Effect of Aerodynamic Constraints on Blade Performance

The actual total power available is dictated by the helicopter power plant which is often limited. Exceeding the power limit may cause severe rotor blade and drive system failure and could be fatal. Therefore, the design of rotor blades demands the consideration of available power limits.

The summary of operating performance parameters against limited power is presented in Table 7. With a limited power of 25 kW (i.e. CP = 0.001) for the AUH, the thrust coefficient would range from 0.0070 to 0.0074 (1.217 kN to 1.286 kN) for untwisted rotor blades. Since the useful range of pitch angles of untwisted blades is 10° to 14°, the maximal thrust coefficient would be extended to CT = 0.01 (1.738

kN) at ptich angles between 16° to 18°, even though the hover efficiency is relatively less than 40%; please refer to Table 8.

With the same power limitations of 25 kW, the thrust coefficient would range 0.0074 to 0.0078 (1.286 kN to 1.356 kN) (Table 7) in the case of twisted blades. The maximal thrust coefficient of CT = 0.01 would be achieved at about θ0.8 = 15◦, which indicates a requirement of 38 kW (CP = 0.00155) of actual power in the twisted case, and the FM would acheive a value of 0.46; see Table 8. At the limited power, the configurations, C2 and C3, are greater in thrust than that of C1, as shown in Table 7. The configuration C3 has an advantage of delayed stall compared with C2 at the maximal thrust conditions.

4. CONCLUSIONS

The aerodynamic design of the rotor blade is evaluated for an agricultural unmanned helicopter (AUH) using the multiple reference frame based Navier-Stokes analysis. Three different blade designs (V1505A (C1), V2008B (C2), and V1215C (C3) are investigated by varying the airfoil shape and twist angle. The performance parameters (thrust, torque, power, and figure of merit) are analyzed at various collective pitch angles in the hovering flight condition for a constant rotational speed. The effect of blade twist on hover performance and spanwise blade loading is also determined. The CFD method is aptly validated by performing the computations for an experimental rotor blade. Moreover, the accuracy of the simulation results is also ensured by a grid sensitivity study, and the effect of turbulence models is also considered.

Both the untwisted and twisted blades with highly cambered airfoil section (V2008B) are aerodynamically more efficient and have the capacity to produce large thrust when compared to blades with relatively thick and less camber airfoil section (V1505A). The realization of high thrust from C2 demands more power to turn the rotor relative to the competing rotor blades. C3 with gradually varying airfoil is relatively less efficient than C2. The superior stall behavior of C3 becomes an ultimate choice to use as the main rotor in the AUH. Moreover, at a limited actual power of the AUH; C2 and C3 produce more thrust than that of C1 with optimal FM values for both the untwisted and twisted cases. In addition, the maximal thrust coefficient is achieved at an angle of 15◦ for the twisted case.

The blade twist plays a key role in delaying the stall, especially near the tip region, which results in the reduction of tip loading. Furthermore, the blade loading becomes more uniform along the blade span when a negative twist is employed. However, a more negative twist is required to attain a better uniform flow distribution. An overall performance gain of 10% is achieved with a blade based on the variable airfoil sections and a linear twist. After development and testing, the rotor blade configuration C3 can be employed with AgroHeli-4G for precision agriculture.

ACKNOWLEDGMENTS

This work is supported by the National Research Foundation of Korea (NRF) funded by the Ministry of Science, ICT & Future Planning (Grant No. 2015R1A2A2A01002328).

REFERENCES

Adeeb, E., A. Maqsood, A. Mushtaq and C. Sohn (2016). Parametric study and optimization of ceiling fan blades for improved aerodynamic performance. *Journal of Applied Fluid Mechanics 9*(6), 2905–2916.

Ahmad, J. and E. P. Duque (1996). Helicopter rotor blade computation in unsteady flows using moving overset grids. *Journal of Air-craft 33*(1), 54–60.

Ansys Design Modeler Release 16.2. ANSYS® Academic Research, Help System, *Design-Modeler User's Guide* . ANSYS, Inc.

Ansys Fluent Release 16.2. ANSYS®Academic Research, Help System, Fluent *Theory and User's Guide* . ANSYS, Inc.

Caradonna, F. and C. Tung (1981). *Experimental and analytical studies of a model helicopter rotor in hover*. Technical Report NASA-TM-81232.

Caradonna, F. X. and M. P. Isom (1972). Subsonic and transonic potential flow over helicopter rotor blades. *AIAA Journal 10*(12), 1606–1612.

Celik, I. B., U. Ghia, P. J. Roache, C. J. Freitas, H. Coleman and P. E. Raad (2008). Procedure for Estimation and Reporting of Uncertainty Due to Discretization in CFD Applications. *Journal of Fluids Engineering 130*(7).

Conlisk, A. T. (2001). Modern Helicopter Aerodynamics. *Progress in Aerospace Sciences 37*, 419–476.

Costes, M., T. Renaud and B. Rodriguez (2012). Rotorcraft simulations: a challenge for CFD. *International Journal of Computational Fluid Dynamics 26*(6-8), 383–405.

di Perta, E. S., M. A. Agizza, G. Sorrentino, L. Boccia and S. Pindozzi (2016). Study of aerodynamic performances of different wind tunnel configurations and air inlet velocities, using computational fluid dynamics (CFD). *Computers and Electronics in Agriculture 125*, 137–148.

Johnson, W. (2013). *Rotorcraft Aeromechanics*. Cambridge University Press.

Koo, Y. M. (2009). *Development of essential mechanical elements for unmanned agricultural helicopter with payload of 20 kg*. Final report for IUPL of SMBA, MOCIE, Daegu, Korea.

Koo, Y. M. (2012). Performance comparison of two airfoil rotor designs for an agricultural unmanned helicopter. *Journal of Biosystems*

Engineering 37(1), 1–10.

Koo, Y. M., T. S. Soek, S. K. Shin, C. S. Lee and T. G. Kang (2006 b). Aerial application using a small RF controlled helicopter (III) – lift test and rotor system. *Journal of Biosystems Engineering 31*(3), 182–187.

Kranzinger, P. P., U. Kowarsch, M. Schuff, M. Keßler and E. Krämer (2016). Advances in parallelization and high-fidelity simulation of helicopter phenomena. In E. W. Nagel, H. D. Kröner, and M. M. Resch (Eds.), *High Performance Computing in Science and Engineering '15: Transactions of the High Performance Computing Center*, Stuttgart (HLRS) 2015, 479–497. Springer International Publishing.

Lee, I.-B., J. P. P. Bitog, S. W. Hong, I. H. Seo, K. S. Kwon, T. Bartzanas and M. Kacira (2013). The past, present and future of CFD for agro-environmental applications. *Computers and Electronics in Agriculture 93*, 168–183.

Lee, S. W. and O. J. Kwon (2006). Aerodynamic shape optimization of hovering rotor blades in transonic flow using unstructured meshes. *AIAA Journal 44*(8), 1816–1825.

Leishman, J. G. (2006). *Principles of Helicopter Aerodynamics*. Cambridge University Press.

Luo, J. Y. and A. Gosmans (1994). Prediction of impeller-induced flows in mixing vessels using multiple frames of reference. *Institute of Chemical Engineers Symposium Series 136*, 549–556.

Meng, T. (2015). Exploration and practice for the agricultural value of unmanned helicopters. *Electronics, Information Technology and Intellectualization* 191–194.

Miller, R. H. (1985). Methods for rotor aerodynamic and dynamic analysis. *Progress in Aerospace Sciences 22*(2), 113–160.

Moin, P. and J. Kim (1997). Tackling turbulence with supercomputers. *Scientific American 276*(2), 62–68.

Pomin, H. and S. Wagner (2002). Navier-stokes analysis of helicopter rotor aerodynamics in hover and forward flight. *Journal of Aircraft 39*(5), 813–821.

Prouty, R. W. (2009). Helicopter Aerodynamics, Helicopter Aerodynamics, Volume I. Lulu.com.

Roache, P. (1994). Perspective: A Method for Uniform Reporting of Grid Refinement Studies. *Journal of Fluids Engineering 116*, 405–413.

Roache, P. (1997). Quantification of uncertainty in computational fluid dynamics. *Annual Review Fluid Mechanics 29*, 123–160.

Senthilnath, J., A. Dokania, M. Kandukuri, R. K. N., G. Anand and S. Omkar (2016). Detection of tomatoes using spectral-spatial methods in remotely sensed RGB images captured by UAV. *Biosystems Engineering 146*, 16–32. Special Issue: Advances in Robotic Agriculture for Crops.

Stafford, J. V. (2000). Implementing precision agriculture in the 21st century. *Journal of Agricultural Engineering Research 76*(3), 267–275.

Sugiura, R., N. Noguchi and K. Ishii (2005). Remote-sensing technology for vegetation monitoring using an unmanned helicopter. *Biosystems Engineering 90*(4), 369–379.

Whelan, B. and J. Taylor (2013). *Precision Agriculture for Grain Production Systems*. Collingwood, Australia.: CSIRO Publishing.

Xia, B. and D. W. Sun (2002). Applications of computational fluid dynamics (CFD) in the food industry: a review. *Computers and Electronics in Agriculture 34*(1-3), 351–374.

Zhang, C. and J. Kovacs (2012). The application of small unmanned aerial systems for precision agriculture: a review. *Precision Agriculture 13*(6), 693–712.

Zhou, J., L. R. Khot, T. Peters, M. D. Whiting, Q. Zhang and D. Granatstein (2016). Efficacy of unmanned helicopter in rainwater removal from cherry canopies. *Computers and Electronics in Agriculture 124*, 161–167.